IEEE Access
Multidisciplinary | Rapid Review | Open Access Journal

Received May 1, 2019, accepted May 20, 2019, date of publication May 27, 2019, date of current version June 10, 2019.

Digital Object Identifier 10.1109/ACCESS.2019.2919140

Magnetic Induction Tomography Using Magnetic Dipole and Lumped Parameter Model

JIYUN JEON, WONMO CHUNG, AND HUNGSUN SON, (Member, IEEE)
Ulsan National Institute of Science and Technology, Ulsan 44919, South Korea

Corresponding author: Hungsun Son (hson@unist.ac.kr)

This work was supported in part by the Ulsan National Institute of Science and Technology (UNIST) through the Future Innovation Research Funds under Grant 1.190011.01, in part by the Development of Multi-Degrees Of Freedom Spherical Motion Platform under Grant 2.190080.01, and in part by the Development of Drone System for Ship and Marine Mission of Civil Military Technology Cooperation Center under Grant 2.180832.01.

ABSTRACT This paper presents a novel approach to analyze the magnetic field of magnetic induction tomography (MIT) using magnetic dipoles and a lumped parameter model. The MIT is a next-generation medical imaging technique that can identify the conductivity of target objects and construct images. It is noninvasive and can be compact in design and, thus, used as a portable instrument. However, it still exhibits inferior performance due to the nonlinearity, low signal-to-noise ratio of the magnetic field, and ill-posed inverse problem. To overcome such difficulties, the magnetic field of the MIT system is first modeled using magnetic dipoles and a lumped parameter. In particular, the extended distributed multipole (eDMP) model is proposed to analyze the system, using magnetic dipoles. The method can dramatically reduce the computational efforts and improve the ill-posed condition. Hence, the forward and inverse problems of MIT are solved using the eDMP method. The modeling method can be validated by comparing with experiments, varying the modeling parameters. Finally, the image can be reconstructed, and then, the position and shape of the object can be characterized to develop the MIT.

INDEX TERMS Extended distributed multipole (eDMP), equivalent circuit modeling, magnetic dipole modeling, magnetic induction tomography (MIT), time-varying magnetic field, eddy current model.

I. INTRODUCTION

Magnetic induction tomography (MIT) is a medical imaging device that uses electromagnetic properties, such as conductivity, to characterize a target object. The existing imaging devices, such as X-ray, CT, and MRI, have been in use for several decades. However, the instruments used in these devices are large and incur high power and cost. In addition, an expert is required to operate the devices, as they can be harmful. In contrast, MIT incurs low power and cost, and thus, is portable and can be used during emergency. In addition, owing to its noninvasive and harmless properties, experts are not required for operation.

A MIT system comprises numerous transmitter coils (Txs) and receiver coils (Rxs). Unknown conductive objects are placed in a region of interest (ROI) and cause magnetic perturbation, as Txs are activated. The perturbation is shown as phase shift at Rxs and analyzed to reconstruct an image. The principle has been utilized in the industry to detect the metal crack for a hundred years [1]. However, as human tissues are extremely low conductivity materials (< 5 S/m), the signal-to-noise ratio (SNR) is also low. Thus, researchers have been trying to improve the performance of MIT since early 90s [2]. Various designs and arrangements of Txs and Rxs have been attempted: multichannel Rxs, changing orientation [3]; hemispherical array [4]; and planar array [5]. In addition, there have been attempts to change the coil type of an Rx, not only a voice coil but also planar coil [6], gradiometer [7]–[9], atomic magnetometer [10], superconducting quantum interference device (SQUID) [1]. To enhance SNR, shielding Txs and Rxs from noise and inserting an iron core into Txs are suggested in [11]. As the conductivity of human tissues depends on frequency, a multifrequency input has been applied to identify the function [4], [8], [12]. Target objects have also been examined from the saline water [13] and agarose [14] administered to rats [15] and rabbits [16], [17]. It is also applied to detect metal for the

The associate editor coordinating the review of this manuscript and approving it for publication was Kezhi Li.

industrial applications, such as steel and alloy [18], [19]. MIT can be combined with existing techniques, such as magneto-acousto-electrical tomography [20] and holography technique [21].

So far, various designs of an MIT system have been developed, but it still shows inferior performance because the magnetic field is intrinsically weak and the analysis of the field is nonlinear and rather complicated. Thus, numerical methods have been utilized to analyze the magnetic field and design MIT systems for high accuracy [22]–[24]. However, the method requires heavy computational effort and contributes to increasing the system volume. Thus, a novel approach demanding fast computation and high accuracy is required to achieve a MIT system. A lumped parameter method is applied to identify and control the system in real time with first-order accuracy. The equivalent circuit model can identify eddy current distribution, and its interaction in tissues [25], [26]. However, this method faces difficulty in describing the detailed characters of the system, such as positions and orientations of Txs and Rxs. Thus, various methods are used to supplement the drawback. For example, in [25], an analytic method computes the induced voltage, and in [26], a numerical method solves the forward problem of MIT. However, combining the analytic and numerical method still requires high computational resource.

The magnetic dipole moment model can analyze the time-varying magnetic field in real time considering the geometry of the system components. The magnetic single-dipole (SD) model is applied to compute the magnetic far-field accurately. The extended distributed multipole (eDMP) method has been proposed to enhance accuracy in the near-field and compute the interaction between magnetic fields, such as magnetic induction, Lorentz force, and torque fast [27]–[29]. In this study, the eDMP method is applied to supplement the equivalent circuit model. The equivalent circuit modeling is applied to identify an entire system of the MIT using Z-parameters. Then, the eDMP can estimate the Z-parameters, considering the properties of the objects and system setup. Once forward modeling is constructed, an inverse algorithm can be developed. Then, conductivity in the ROI can be determined by solving the inverse of phase shift and image processing can be achieved.

The experiments are performed to demonstrate the method is applicable to a MIT system. The object with uniform conductivity is applied as illustration and the effect of the object properties is studied since it requires high sensitivity for variation in the properties.

The remainder of this paper is organized as follows: First, the eDMP model and the equivalent circuit model are applied to modeling MIT. The modeling method is compared with experiments and other simulation method varying the object properties for validation. Then, the image is reconstructed to characterize the object in the ROI. The results can estimate the applicability of the eDMP method to MIT.

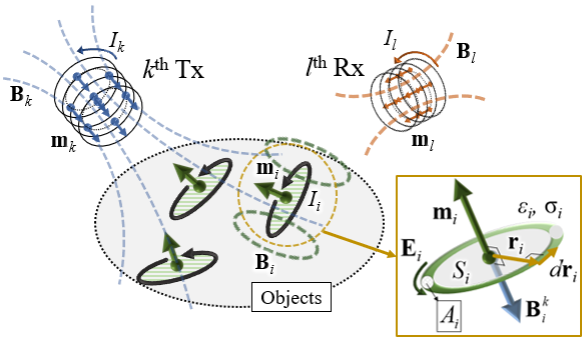

FIGURE 1. eDMP model of MIT.

II. MIT MODEL

A. MAGNETIC FIELD OF MIT

In Fig. 1, a pair of a k^{th} transmitter (Tx) coil ($k = 1, \ldots, N_k$) and a l^{th} receiver (Rx) coil ($l = 1, \ldots, N_l$) and conducting objects are shown for the illustration of the fundamental of MIT. The i^{th} object ($i = 1, \ldots, N_i$) has conductivity σ_i and permittivity ε_i. As the Tx coil generates time-harmonic magnetic flux density $\mathbf{B}_k$(blue dashed line), the electric field $\mathbf{E}_i$ (green curved arrow) is induced in the i^{th} object and estimated as

$$\nabla \times \mathbf{E}_i = -\frac{\partial \mathbf{B}_k}{\partial t} = -j\omega \mathbf{B}_k \tag{1}$$

where $j^2 = -1$ and ω is the operating angular frequency.

The current I_i (green loop) which is caused by $\mathbf{E}_i$ and σ_i generates the secondary magnetic field $\mathbf{B}_i$(green dashed line), whose phase is different from that of the primary field. The Rx coil can identify the phase shifted by the secondary field, and the phase shift depends on conductivity, relative orientation, and position among Tx, Rx, and the object. Thus, conductivity distribution in the ROI can be obtained by analyzing the phase shift.

The eDMP model utilizes multiple magnetic dipole moments to describe a coil and analyze the magnetic field. The number, arrangement, and strength of dipole moments are optimized, considering the design of a coil [29]. Magnetic vector potential $\mathbf{A}$, flux density $\mathbf{B}$ and mutual inductance between two coils can be computed using the dipole moments in Appendix (A.1-A.3). Fig. 1 shows the eDMP applied to the MIT. Two coils, as Tx and Rx, are modeled with the dipole moments $\mathbf{m}_k$ (blue arrows) and $\mathbf{m}_l$ (brown arrows), with current input I_k(blue curved arrow) and I_l (brown curved arrow), respectively. Unlike Tx and Rx, the objects can take various shapes, but not that of a coil. Thus, it is assumed that the object comprises numerous single-turn coils. The i^{th} object coil carrying current I_i has a loop with radius r_i ($= ||\mathbf{r}_i||$) and the cross-section area A_i of coil winding. Furthermore, the loop is composed of a material with σ_i and ε_i. Each single-turn coil is represented as an SD moment, $\mathbf{m}_i$ (green arrow).

For the given design of Tx and Rx coils, the orientation and strength of $\mathbf{m}_i$ can be computed using (1) and (A.2). As in (1), the induced field $\mathbf{E}_i$ in the coil of I_i becomes perpendicular to

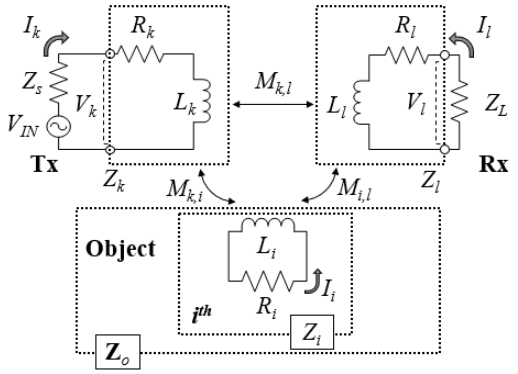

FIGURE 2. Equivalent circuit model of the MIT system.

the primary field at the i^{th} object,$\mathbf{B}_i^k$, which can be assumed to be uniform within the loop area S_i ($=\pi r_i^2$), encircled by the current, particularly for a small r_i. Then, (1) can be converted to (2) for the i^{th} object.

$$\oint_{\gamma_i} \mathbf{E}_i \cdot d\mathbf{r}_i = -\iint_{S_i} \frac{\partial \mathbf{B}_i^k}{\partial t} \cdot \mathbf{n}_i dS_i \tag{2}$$

$$\oint_{\gamma_i} \mathbf{E}_i \cdot d\mathbf{r}_i = 2\pi r_i \left\|\mathbf{E}_i\right\| \tag{2a}$$

$$-\iint_{S_i} \frac{\partial \mathbf{B}_i^T}{\partial t} \cdot \mathbf{n}_i dS_i = -j\omega\pi r_i^2 \left\|\mathbf{B}_i^k\right\| \tag{2b}$$

where t is time; $\mathbf{n}_i$ is the unit normal vector of S_i; $d\mathbf{r}_i$ is the unit tangent vector of loop I_i; and the negative sign follows Lenz's law.

Based on the orientations of $\mathbf{E}_i$ and I_i, the dipole moment $\mathbf{m}_i$ per unit I_i can be obtained as (3), following the definition of the magnetic single dipole moment.

$$\mathbf{m}_i / I_i = \oint_{\gamma_i} \mathbf{r}_i \times d\mathbf{r}_i = \pi r_i^2 \mathbf{B}_i^k \Big/ \left\|\mathbf{B}_i^k\right\| \tag{3}$$

The strengths of I_i and $\mathbf{m}_i$ can be determined as functions of σ_i and ε_i using Ohm's law. Thus, the equivalent circuit model is applied to solve Ohm's law in the objects. Furthermore, the circuit model can compute the phase shift considering the source of Tx and load of Rx. Fig. 2 shows the equivalent circuit model of the MIT system shown in Fig. 1. The coils of Tx and Rx are represented as the *RL* circuit, composed of resistance R_k, R_l and self-inductance L_k, L_l, respectively and have source impedance Z_S and load impedance Z_L. The *RL* circuit is used to model the i^{th} object with resistance R_i and self-inductance L_i. Each circuit is connected through the mutual inductances $\mathrm{M}_{k,i}$, $\mathrm{M}_{i,l}$, and $\mathrm{M}_{k,l}$ between Tx and the object, Rx and the object, and Tx and Rx, respectively. As the Tx is activated by time-harmonic input V_{IN}, the Z-parameter of the MIT system can be expressed as (4-4b).

$$\begin{bmatrix} V_{IN} \\ 0 \\ \mathbf{0}_{N_i \times 1} \end{bmatrix} = [\mathbf{Z}] \begin{bmatrix} I_k \\ I_l \\ \mathbf{I}_o \end{bmatrix} \tag{4}$$

$$[\mathbf{Z}] = \begin{bmatrix} Z_s + Z_k & j\omega M_{k,l}^{\mathrm{T}} & j\omega \mathbf{M}_{k,o}^{\mathrm{T}} \\ j\omega M_{k,l} & Z_l + Z_L & j\omega \mathbf{M}_{l,o}^{\mathrm{T}} \\ j\omega \mathbf{M}_{k,o} & j\omega \mathbf{M}_{l,o} & \mathbf{Z}_o \end{bmatrix} \tag{4a}$$

$$Z_a = R_a + j\omega L_a \ (a = k, l, i) \tag{4b}$$

where $\mathbf{M}_{k,o} = [M_{k,1} \ldots M_{k,Ni}]^{\mathrm{T}}$; $\mathbf{M}_{l,o} = [M_{l,1} \ldots M_{l,Ni}]^{\mathrm{T}}$; $Z_o = Z_i \mathbf{I}$; and $\mathbf{I}_o = [I_1 \ldots I_{Ni}]^{\mathrm{T}}$.

The circuit parameters of the objects modeled as a single-turn coil, R_i and L_i, can be computed using the coil design shown in Fig. 1. R_i is estimated with complex conductivity κ_i ($=\sigma_i + j\omega\varepsilon_i$), as shown in (5).

$$R_i = \frac{2\,pir_i}{\kappa_i A_i} \tag{5}$$

The self-inductance of an object is defined as the magnetic flux passing through the current loop area per unit current and hence, L_i is obtained in (6), using (A.4-A.6). Finally, Z_i in (4b) is expressed as in (7).

$$L_i = \pi r_i^2 \left\|\mathbf{B}_i\right\|_{S_i} \Big/ I_i = \mu_0 \pi r_i / 2 \tag{6}$$

$$Z_i = \frac{2\pi r_i}{(\sigma_i + j\omega\varepsilon_i) A_i} + j\omega \frac{\mu_0 \pi r_i}{2} \tag{7}$$

The mutual inductances in (4a) can be computed by substituting $\mathbf{m}_k$, $\mathbf{m}_l$, and$\mathbf{m}_i$ in (A.3). Then, the impedance $\mathbf{Z}$ in (4) can be estimated using (2)−(7). As in (8), V_{kl0} and ΔV_{kl} are the voltages induced on Z_L due to the Tx and objects, respectively. The phase shift by the objects, $\Delta\varphi_{kl}$, is obtained in (9).

$$V_{kl0} + \Delta V_{kl} = -\frac{Z_L}{Z_l + Z_L} \left(j\omega M_{k,l} I_k + j\omega \mathbf{M}_{l,o}^{\mathrm{T}} \mathbf{I}_o\right) \tag{8}$$

$$\Delta\varphi_{kl} = \angle \left(\frac{V_{kl0} + \Delta V_{kl}}{V_{kl0}}\right) = \tan^{-1} \left(\frac{\mathbf{M}_{l,o}^{\mathrm{T}} \mathbf{I}_o}{M_{k,l} I_k}\right) \tag{9}$$

B. CONDUCTIVITY ESTIMATION OF MIT

Fig. 3 shows that the number of Txs, N_k, and number of Rxs, N_l, are applied to the plane ROI with radius R_{ROI}. The Txs and Rxs surround the ROI, with radii R_{T} and R_{R}, respectively. It is crucial to measure several effective measurements from Rxs and estimate the conductivity of the number of objects, N_i, minimizing the ill-posed condition. In general, a Tx is energized with various input frequencies, and then, the phase shift is measured at every Rx due to the object. The various fields can be formed by activating the Tx arrangement with respect to the object and Rxs.

The mutual inductance $\mathbf{M}_{l,o}$in the third row of (4a) can be neglected since the effect of the magnetic field from the Rx coil on the object is small as the Rx yields a relatively weak field compared to the Tx coil. Thus, each eddy current I_i becomes directly proportional to $M_{k,i}$ and is expressed using admittance Y_i ($=1/Z_i$) in (10).

$$I_i = -j\omega M_{k,i} I_k / Z_i = -j\omega M_{k,i} I_k Y_i \tag{10}$$

The voltage induced from the objects to the l^{th} Rx is a linear combination of Y_i, as shown in (11). Subsequently, the phase

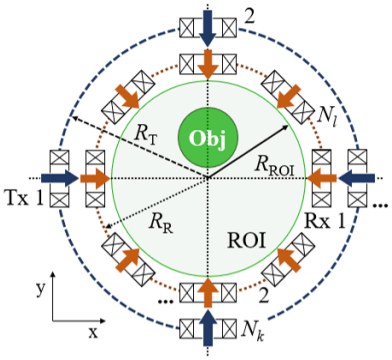

FIGURE 3. Design of the MIT system with multiple Txs and Rxs.

shift $\Delta\varphi_{kl}$ at the l^{th} Rx is computed by substituting (11) for (9), in (12).

$$j\omega \mathbf{M}_{l,o}^{\mathrm{T}} \mathbf{I}_o = \omega^2 \sum_{i=1}^{N_i} M_{l,i} M_{k,i} I_k Y_i \tag{11}$$

$$\tan(\Delta\varphi_{kl}) = -j\omega \sum_{i=1}^{N_i} M_{l,i} M_{k,i} Y_i \Big/ M_{k,l} \tag{12}$$

For each Tx and Rx, the phase shift due to the admittance $\mathbf{Y}_o$ can be expressed using the sensitivity matrix $\mathbf{P}$.

$$\tan(\Delta\boldsymbol{\varphi}) = [\mathbf{P}]\,\mathbf{Y}_o \tag{13}$$

$$\mathbf{P} = \left[\, \mathbf{P}_{1,Ro}^{\mathrm{T}} \quad \cdots \quad \mathbf{P}_{k,Ro}^{\mathrm{T}} \quad \cdots \quad \mathbf{P}_{N_k,Ro}^{\mathrm{T}} \,\right]^{\mathrm{T}} \tag{13a}$$

$$\mathbf{P}_{k,Ro} = \begin{bmatrix} \cdots & (l-1)^{th} & \cdots \\ (i-1)^{th} & -\dfrac{j\omega M_{l,i} M_{k,i}}{M_{k,l}} & (i+1)^{th} \\ \cdots & (l+1)^{th} & \cdots \end{bmatrix} \tag{13b}$$

where $\mathbf{Y}_o = [\, 1/Z_1 \ldots 1/Z_{Ni}]^{\mathrm{T}}$; $\Delta\boldsymbol{\varphi} = [\Delta\boldsymbol{\varphi}_{1R}^{\mathrm{T}} \ \ldots \ \Delta\boldsymbol{\varphi}_{NkR}^{\mathrm{T}}]^{\mathrm{T}}$; $\Delta\boldsymbol{\varphi}_{kR} = [\Delta\boldsymbol{\varphi}_{k1} \ \ldots \ \Delta\boldsymbol{\varphi}_{kNl}]^{\mathrm{T}}$; $\mathbf{P}_{k,Ro} \in \mathbb{C}^{N_l \times N_i}$; and $\mathbf{P} \in \mathbb{C}^{(N_k N_l) \times N_i}$.

The admittance $\mathbf{Y}_o$ can be computed by solving inverse of (13), using Tikhonov regularization in (14). Finally, the conductivity can be estimated in (15).

$$\mathbf{Y}_o = \left(\mathbf{P}^{\mathrm{T}}\mathbf{P} + \lambda \mathbf{I}\right)^{-1} \mathbf{P}^{\mathrm{T}} \tan\left(\Delta\boldsymbol{\varphi}_R\right) \tag{14}$$

$$\sigma_i = Re\left(\frac{2\pi\gamma_i}{(Z_i - j\omega L_i)\, A_i}\right) \tag{15}$$

where λ is the scalar regularization parameter.

C. EFFECT OF OBJECTS ON MAGNETIC FIELD

The magnetic field in the ROI is initially parallel to the primary field by $\mathbf{m}_i$ of Txs without an object. Once the object is placed in the ROI, the field would be changed by the secondary field generated by the object dipoles. The original primary field should be reflected by the secondary field, which can be iteratively computed to converge to a steady-state field. At the $(n\text{-}1)^{\text{th}}$ iteration step, the i^{th} object current I_i^{n-1} and dipole $\mathbf{m}_i^{n-1}$ are computed by (4) after (14). Then, the secondary field and total field on the i^{th} object at the n^{th} computation, $\mathbf{B}_i^{o,n}$ and $\mathbf{B}_i^{k,n}$, can be estimated as shown in (16) and (17). Consequentially, the direction of $\mathbf{m}_i$ is rearranged according to (18) and the conductivity can be accurately updated by repeating (4)–(15). The iteration is proceeded until the dipole moments converge. The entire procedure is summarized in Fig. 4.

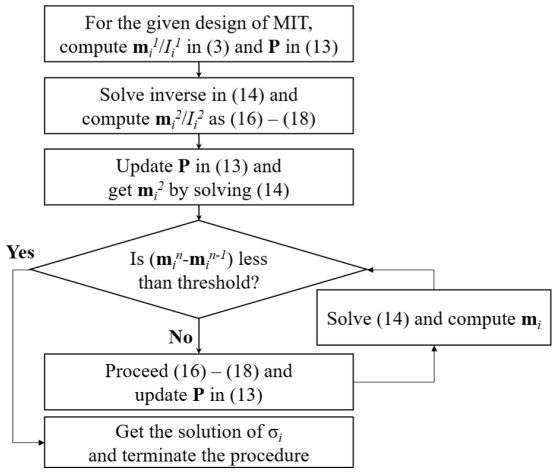

FIGURE 4. Flowchart of eDMP modeling for MIT.

$$\mathbf{B}_i^{o,n-1} = \frac{\mu_0}{4\pi} \sum_{\substack{h=1 \\ (h \neq i)}}^{N_i} \frac{\left(\mathbf{m}_h^{n-1} \cdot \hat{\mathbf{r}}_{i,h}\right) \hat{\mathbf{r}}_{i,h} - \mathbf{m}_h^{n-1}}{\left|\mathbf{r}_{i,h}\right|^3} \tag{16}$$

$$\mathbf{B}_i^{k,n} = \mathbf{B}_i^{k} + \mathbf{B}_i^{o,n-1} \tag{17}$$

$$\mathbf{m}_i^n / I_i^n = \pi r_i^2 \mathbf{B}_i^{k,n} \Big/ \left\| \mathbf{B}_i^{k,n} \right\| \tag{18}$$

III. NUMERICAL SIMULATION AND EXPERIMENTS

The performance of MIT is estimated by examining the effects of conductivity, position, and shape of objects. First, the numerical simulations of both eDMP and finite-difference time domain (FDTD) methods are conducted, and then, the results are compared to the experiment results. Each experiment is repeated three times for reliability. The mean and standard deviation of the results are presented.

A. MIT SYSTEM SETUP

The MIT system is constructed for experiments with one set of a Tx and Rx, as shown in Fig. 5(a), and shielded from the external magnetic field. The geometry of the system and the design of the Tx and Rx are detailed in Tables 1 and 2, respectively.

Physiological saline similar to the human body fluid is applied to the object. At room temperature, the salt concentration is 0.9 %, conductivity is 1.6 S/m, and relative permittivity is 80. Two shapes, circle and square, are used as the target object to examine the effect of shape. Physiological saline 40 ml is injected in a circle and square case in Fig. 5(b) and (c).

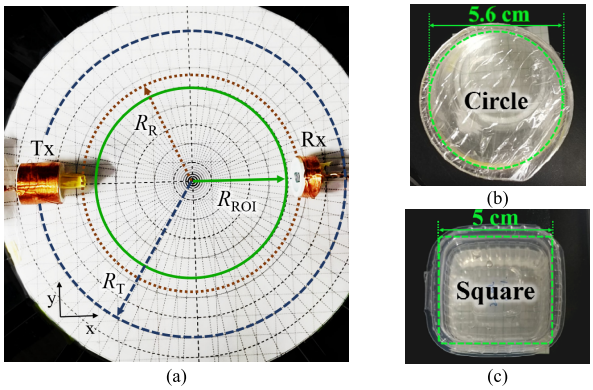

FIGURE 5. Picture of (a) MIT system: (b) circle and (c) square objects.

TABLE 1. Geometry of the MIT System.

R_T (cm)	7.6
R_R (cm)	5.6
R_{ROI} (cm)	5.0

TABLE 2. Coil design.

	Tx	Rx
Radius (cm)	1.0	1.0
Height (cm)	2.0	1.0
Number of turns	60	18
Diameter of wire (mm)	0.3	0.5
Resistance (Ω)	0.5	0.2
Inductance (μH)	20	8.5

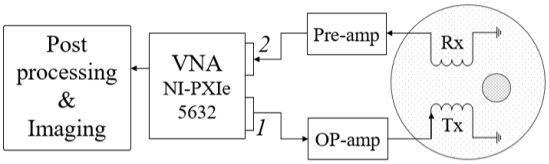

FIGURE 6. Block diagram of the MIT system.

The experimental setup for the measurement is represented by the block diagram shown in Fig. 6. The NI pxie-5632 vector network analyzer (VNA) is used to measure the S-parameters of the device under test, with bandwidth of 300 kHz to 8.5 GHz.

B. NUMERICAL SIMULATION

The FDTD method is used to estimate and compare the performance of MIT. Unlike other numerical methods based on the frequency domain, FDTD is simulated in time domain based on the partial differential form of Maxwell's equations, so that a wide range of frequencies can be calculated simultaneously. FDTD has been applied to a range of systems, from ultralow frequency to visible light, due to the advantage of time-domain simulation and effectiveness.

Fig. 7(a) and (b) show that FDTD is applied to the MIT system in Fig. 5(a) and a square ROI of 28.8 cm × 28.8 cm × 15.8 cm is divided by 204, 204, and 74 cells in the x-, y-, and z-axes, respectively. At the end of each axis, eight lines of the perfect matched layer are placed for absorbing the boundary condition. As the method requires a large computational resource due to the enormous number of meshes, for accuracy, it is performed using a computer with INTEL quad-core i7 and 3.30 GHz CPU.

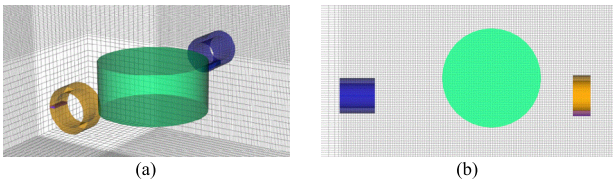

FIGURE 7. FDTD model of the MIT system in (a) 3D and (b) x-y plane.

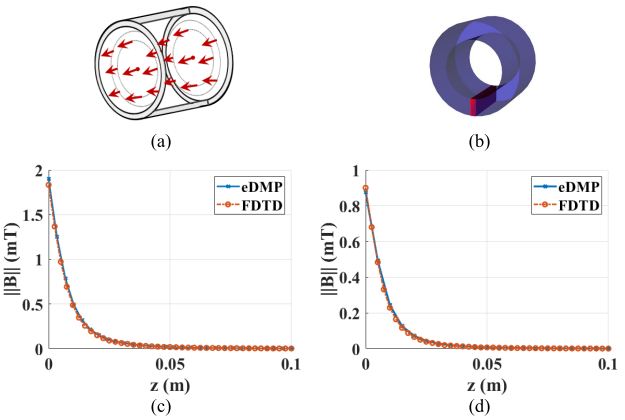

FIGURE 8. (a) eDMP model of a coil. (b) FDTD model of a coil. ||B|| comparison of (c) Tx and (d) Rx.

Similarly, the eDMP method is applied in Fig. 8(a) based on the coil design in Table 2. In Fig. 8(b), the magnetic field generated by Tx is compared to that generated by FDTD for validation. In Figs. 8(c) and (d), the magnetic flux density **B** per current along the central axis of the Tx and Rx is computed, 10 cm from the surface of the coil, and the eDMP is compared with the FDTD. The mean discrepancy between the eDMP and FDTD is 0.0013 and 0.0044 mT.

For the object modeling, the triangular distribution of object dipoles is used, since it can effectively account for various object shapes. Thus, object dipoles are arranged to form uniform regular triangles. Then, the following dipole parameters should be determined: r_i, N_i, and A_i. r_i in (3) can be set as half the length of the triangle to prevent overlapping between nearby dipoles. N_i should be large enough to describe the object shape and the primary field in the ROI. However, an excessively large N_i increases the computational effort. Fig. 9(a) shows that the total induced voltage in the plane ROI per unit Tx current converges as N_i increases. It is confirmed that the number larger than 1000 results in steady computation. Considering the computation resource, N_i is set as 1270 and r_i is set as 3 mm. It is difficult to estimate A_i accurately since the eddy current in the objects cannot be observed directly. But, A_i can be removed by normalizing phase shift. Finally, the eDMP model of the MIT system in Fig. 5(a) can be presented in Fig. 9(b-c), where single

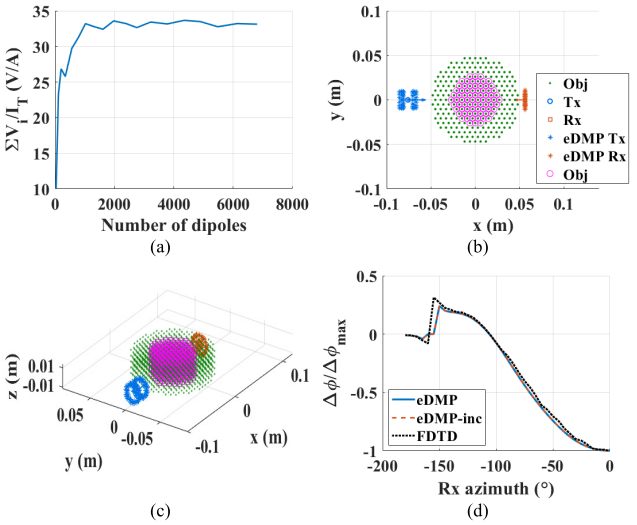

FIGURE 9. (a) Induced voltage in the ROI. eDMP model of the MIT system (b) in x-y plane and (c) 3D view. (d) Comparison of phase shift.

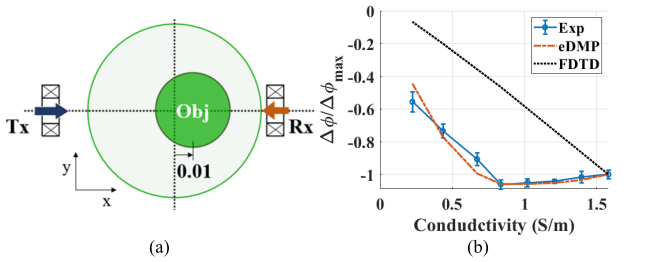

FIGURE 10. Phase shift as conductivity changes: (a) design and (b) results.

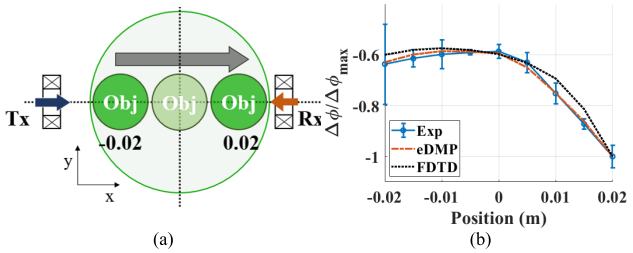

FIGURE 11. Phase shift as object moves: (a) design and (b) result.

arrows indicate orientation of the coil. The object dipoles corresponding to the saline in Fig. 5(b) are represented as pink circles. Phase shift in the model can be computed using (13). In Fig. 9(d), the phase shift, varying the Rx azimuth angle from −180 to 0°, is validated by comparing with other methods: the eDMP method including the mutual inductances between objects, Rxs and objects, in (4) and FDTD method. The phase shift in the results is normalized to the maximum of each result for comparison. It yields mean discrepancy 0.00003 with the eDMP including every term and 0.0096 with FDTD. Thus, it is confirmed that the eDMP method can be applied to compute phase shift using (13).

The operating frequency should be considered to enhance the system performance. The maximum allowable frequency for MIT is 30 MHz, due to β-dispersion in the living tissue, whereas increasing the frequency can amplify the phase shift, as shown in (13). In addition, the impedance of Tx is proportional to the frequency, as shown in (4b), and the increment in Tx impedance can reduce the SNR. Impedance matching can reduce the impedance at the specific frequency. The Rx circuit can be ignored because the phase shift does not depend on I_l in (13). Thus, for the design of a Tx coil in Table 2, the Tx circuit is tuned to operate at 24 MHz.

C. EFFECT OF CONDUCTIVITY VARIATION

In the human body, conductivity varies from 0.02 to 1.5 S/m. Blood conductivity is 1.14 S/m, muscle is 0.64, skin is 0.29, and bone is 0.02 [30]. Thus, the conductivity resolution of MIT should be high enough to determine the type of tissues. The MIT system is set in Fig. 10(a). The circular object is placed at (0.01, 0) m, varying the conductivity within the range of human tissue, from 0.2 to 1.6 S/m. The trend in the phase shift due to conductivity variation is consistent in every setup; thus, without loss of generality, the result can be taken in other setups. In Fig. 10(b), the experimental result is normalized with respect to a point at 1.6 S/m and compared to the simulation results, yielding a mean error of 0.0341 with eDMP and 0.3849 with FDTD. For low conductivity (<0.8 S/m), the phase shift increases with the conductivity. However, for a conductivity above 0.8 S/m, the phase shift decreases. In (4-4b), high conductivity reduces R_i, and then, self-inductance $j\omega L_i$ becomes dominant in $\mathbf{Z}_o$ and the phase shift decreases. In FDTD, the phase shift is linear as the conductivity increases, because only resistance is considered. It is confirmed that the conductivity can be estimated from the phase shift within the tissue range.

D. EFFECT OF POSITION

Phase shift, as the object position, indicates the spatial accuracy and resolution. In Fig. 11(a), the system design is shown to move the object from −0.02 to 0.02 m, along the x-axis. The experimental result is compared to the simulation result in Fig. 11(b), yielding a mean error of 0.0086 with eDMP and 0.0260 with the FDTD method. As the position changes from 0 to 0.02 m, the phase shift increases, and then, the position becomes distinguishable. However, within (−0.02-0) m, it is difficult to determine the position because the sensitivity in (13) is uniform within the region. Arranging the Tx and Rx on a symmetrical position can improve the spatial resolution in the region. Thus, numerous Txs and Rxs should be placed at various locations to enhance sensitivity in the entire ROI.

The relative position between the Tx and Rx can achieve the same performance as that obtained using multiple Txs and Rxs, as shown in Fig. 3. Thus, the Tx is placed at every 90° ($N_k = 4$) and the Rx is arranged every 5°, from −90° to 265° ($N_l = 72$). In total, 288 phase shifts are acquired in the system. The circular object is placed at (0, 0.01) m and the eDMP model of the circle is shown in Fig. 12(a). The phase shifts are arranged in Fig. 12, at (b) Tx1, (c) Tx2, and (d) Tx4, and normalized with respect to the maximum in Fig. 12(b)−(d).

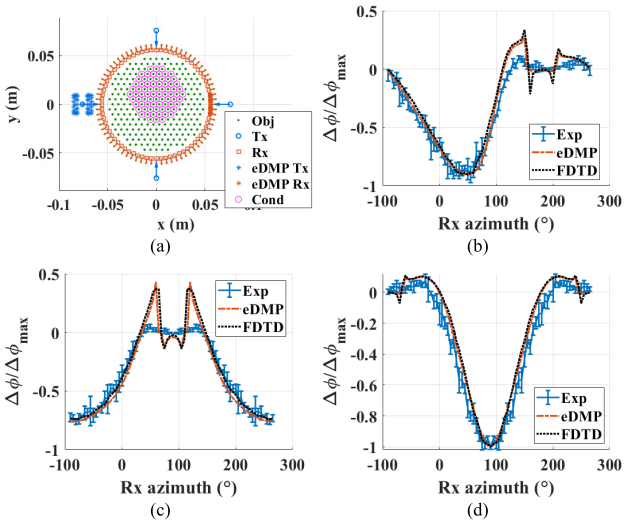

FIGURE 12. (a) eDMP model with multiple Txs and Rxs; phase shifts at (b) Tx1, (c) Tx2, and (d) Tx4.

TABLE 3. Mean error of simulations in fig. 12.

Figure	(b)	(c)	(d)
eDMP	0.0528	0.0656	0.0669
FDTD	0.0749	0.0675	0.0774

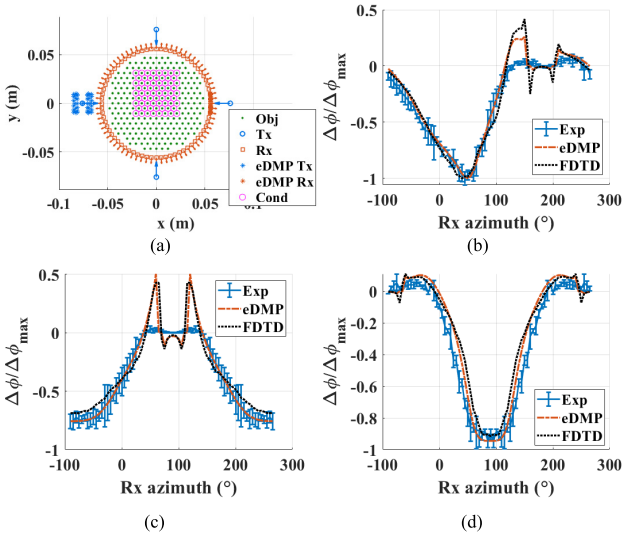

FIGURE 13. (a) eDMP model of square; phase shifts at (b) Tx1, (c) Tx2, and (d) Tx4.

The result at Tx3 is excepted since it is symmetrical to that at Tx1. The mean errors are listed in Table 3. In the simulation results, there are sharp peaks and discontinuities, such as Rx azimuth 150 and 210° in Fig. 12(b), 60 and 120° in Fig. 12(c). As an Rx coil is arranged perpendicular to the primary field, $M_{k,l}$ in (13b) becomes small which result in discontinuities. In the experiments, the peaks are not observed because there is a bias voltage on Rx. Except for the few points, the phase shift is shown clearly as Txs and Rxs change. In addition, the position of the object can be characterized in the results.

TABLE 4. Mean error of simulations in fig. 13.

Figure	(b)	(c)	(d)
eDMP	0.0554	0.0470	0.0704
FDTD	0.0789	0.0970	0.0872

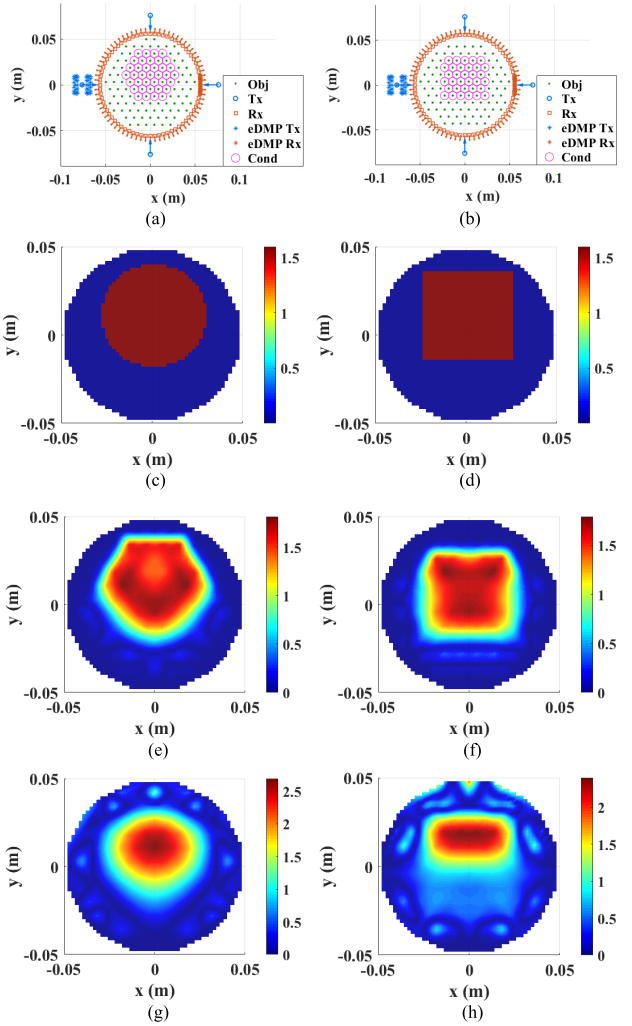

FIGURE 14. Imaging results with $r_i = 4.5$ mm. eDMP model of (a) circle and (b) square; true image of (c) circle and (d) square; simulation results of (e) circle and (f) square; experimental results of (g) circle and (h) square.

For example, the maximum phase shift in Fig. 12(c) is less than the maximum in Fig. 12(d), as shown in Fig. 11(b).

E. EFFECT OF SHAPE

Various shapes of a target object are required to characterize the type of tissues with similar conductivity. Fig. 13(a) shows the eDMP model with the square object in Fig. 5(c) placed at (0, 0.01) m to compare to the circle Fig. 13(b)−(d) presents the results, yielding the mean errors as listed in Table 4. The phase shift in Fig. 13 is similar to that in Fig. 12, and has sharp peaks. Nevertheless, several differences are observed; the phase shift in Fig. 13(b) has a higher gradient and sharper maximum than that in Fig. 12(b). In addition, in Fig. 13(d), the phase shift shows a blunt shape at the

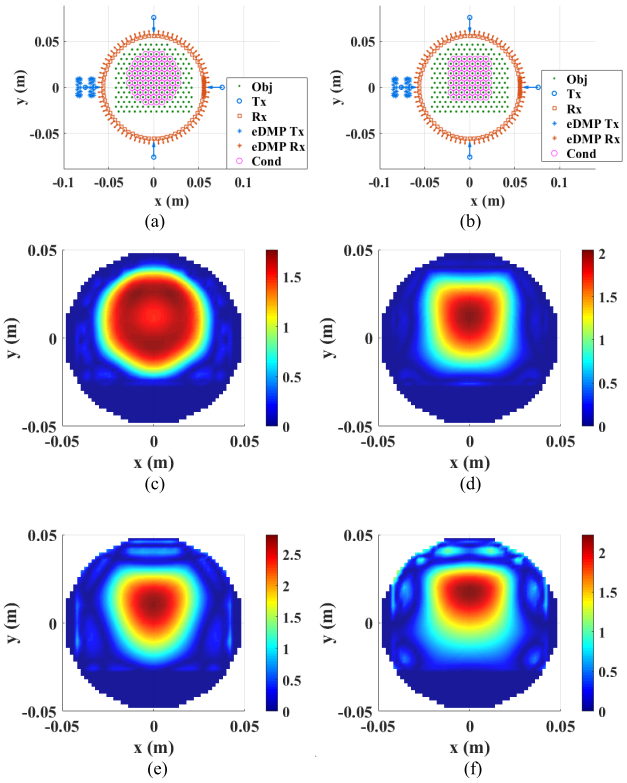

FIGURE 15. Imaging results with $r_i = 3$ mm. eDMP model of (a) circle and (b) square; simulation results of (c) circle and (d) square; experimental results of (e) circle and (f) square.

maximum, while the result of circle is sharp in Fig. 12(d). It is confirmed that the MIT system can detect the object shape in phase shift.

F. IMAGE RECONSTRUCTION

The image reconstruction can be achieved by solving the inverse in (14), using the results in Figs. 12 and 13. Considering that large N_i causes an ill-posed condition, in Fig. 14(a) and (b), the object dipoles of the eDMP models are rearranged as r_i is 4.5 mm and N_i is 456. True images are shown in Fig. 14(c) for the circle and (d) for the square. Fig. 14(e)−(f) is based on the eDMP simulation and Fig. 14(g)−(h) shows the experimental results. In Fig. 14(f), Tikhonov regularization coefficient in (14) is computed from the circle as a reference object for calibration and the corresponding coefficient is applied to the square in Fig. 14(h). The final images are scaled to the absolute value for comparison. The simulation images show that the position and conductivity of the object corresponds with that of the true image and the object shape is distinguishable. But the results have the same resolution as that of the eDMP model shown in Fig. 14(a)−(b), and thus, show coarser resolution than those of the true and experimental images. In the experimental images, the position of the objects corresponds with that of the true image. But conductivity is not uniform due to the measurement error in Fig. 12. The object shape is characterized: the circle in Fig. 14(g) maintains curvature uniformly but has a smaller size than the true image. In Fig. 14(h), the square has four edges, but the aspect ratio is less than one.

The image resolution can be improved by increasing the object dipoles in the vicinity of the object. In Fig. 15(a) and (b), the eDMP models with r_i reduced from 4.5 mm to 3 mm are shown. In addition, dipoles 4 cm away from the object center are eliminated to improve the ill-posed condition. Thus, 995 dipoles are applied to describe the object shape. Consequently, the simulation results in Fig. 15(c) and (d) show higher resolution than those in Fig. 14(e) and (f). The experimental results are shown in Fig. 15(e) and (f). The circle in Fig. 15(e) is distorted more than that in Fig. 14(g), but its size grows similar to the true image in Fig. 14(c). In Fig. 15(f), the aspect ratio of the square becomes one. Eventually, the results show that the MIT using the eDMP can be applied to reconstruct images to detect the conductivity, position, and shape of the object.

IV. CONCLUSION

In this study, a MIT was developed using the eDMP method for modeling and applied to detect a low conductivity object. The eDMP method utilized several dipoles for the objects to estimate the magnetic coupling between the coils and objects. The equivalent circuit modeling was applied to analyze the phase shift in the MIT system, considering the object properties. An inverse algorithm was applied using Tikhonov regularization. The phase shifts in the experiments, eDMP and FDTD numerical method were compared. The results showed good agreement as the conductivity, position, and shape of the object were changed. Images were reconstructed and refined to present the properties of a circle and a square. Finally, it is expected that the eDMP method and lumped parameter model contribute to develop an MIT system and achieve better performance. In future research, the system design will be improved using the method to enhance sensitivity.

APPENDIX

Magnetic vector potential $\mathbf{A}$ and flux density $\mathbf{B}$ at an arbitrary position $\mathbf{r}$ are computed using eDMP model $\mathbf{m}_a$, in (A.1-A.2) [29]. The mutual inductance between $\mathbf{m}_a$ and $\mathbf{m}_b$, $M_{a,b}$, is expressed as (A.3) [27], where subscripts a and b can be a transmitter, a receiver, and objects.

$$\mathbf{A}(\mathbf{r}) = \frac{\mu_0 I_a}{4\pi} \sum_{n=1}^{N_a} \frac{(\mathbf{m}_{an}/I_a) \times \mathbf{r}_n}{\|\mathbf{r}_n\|^3} \tag{A.1}$$

$$\mathbf{B}(\mathbf{r}) = \frac{\mu_0 I_a}{4\pi} \sum_{n=1}^{N_a} \frac{\left[3\left(\mathbf{m}_{an}/I_a \cdot \hat{\mathbf{r}}_n\right)\hat{\mathbf{r}}_n - \mathbf{m}_{an}/I_a\right]}{\|\mathbf{r}_n\|^3} \tag{A.2}$$

$$M_{a,b} = \frac{1}{I_a I_b}\left(\sum_{n=1}^{N_a} \mathbf{m}_{an} \cdot \mathbf{B}_{an}^b\right) = M_{b,a} \tag{A.3}$$

where μ_0 is the permeability of air; $\hat{\mathbf{r}}_n = \mathbf{r}_n / \|\mathbf{r}_n\|$; $\mathbf{m}_a = [\mathbf{m}_{a1} \ldots \mathbf{m}_{aNa}]$; N_a is the number of dipole moments of coil a; $\mathbf{r}_n$ is the relative position from the position of $\mathbf{m}_{an}$ to $\mathbf{r}$; and $\mathbf{B}_a^b$ is the flux density of $\mathbf{m}_b$ at the position of $\mathbf{m}_a$.

The magnetic flux density in (6) can be converted to vector potential $\mathbf{A}_i$ on the loop of I_i, as shown in (A.4). $\mathbf{A}_i$ can be computed by substituting $\mathbf{m}_i$ in (A1), and hence, L_i in (4b) is obtained as

$$L_i = \pi r_i^2 \, \|\mathbf{B}_i\|_{S_i} \Big/ I_i = 2\pi r_i \, \|\mathbf{A}_i\|_{r_i} \Big/ I_i \quad \text{(A.4)}$$

$$(\mathbf{A}_i/I_i)|_{\mathbf{r}=\mathbf{r}_i} = \frac{\mu_0}{4\pi} \frac{(\mathbf{m}_i/I_i) \times \mathbf{r}_i}{r_i^3} = -\frac{\mu_0}{4} d\mathbf{r}_i \quad \text{(A.5)}$$

$$L_i = \mu_0 \pi r_i \big/ 2. \quad \text{(A.6)}$$

REFERENCES

[1] J. García-Martín, J. Gómez-Gil, and E. Vázquez-Sánchez, "Non-destructive techniques based on eddy current testing," *Sensors*, vol. 11, no. 3, pp. 2525–2565, Feb. 2011.

[2] H. Griffiths, "Magnetic induction tomography," *Meas. Sci. Technol.*, vol. 12, no. 8, pp. 1126–1131, Jun. 2001.

[3] D. Gürsoy and H. Scharfetter, "The effect of receiver coil orientations on the imaging performance of magnetic induction tomography," *Meas. Sci. Technol.*, vol. 20, no. 10, Sep. 2009, Art. no. 105505.

[4] M. Zolgharni, H. Griffiths, and P. D. Ledger, "Frequency-difference MIT imaging of cerebral haemorrhage with a hemispherical coil array: Numerical modelling," *Physiol. Meas.*, vol. 31, no. 8, pp. S111–S125, Jul. 2010.

[5] C. H. Igney, S. Watson, R. J. Williams, H. Griffiths, and O. Dössel, "Design and performance of a planar-array MIT system with normal sensor alignment," *Physiol. Meas.*, vol. 26, no. 2, pp. S263–S278, Mar. 2005.

[6] C. H. Riedel, M. Keppelen, S. Nani, R. D. Merges, and O. Dössel, "Planar system for magnetic induction conductivity measurement using a sensor matrix," *Physiol. Meas.*, vol. 25, no. 1, pp. 403–411, Feb. 2004.

[7] B. U. Karbeyaz and N. G. Gencer, "Electrical conductivity imaging via contactless measurements: An experimental study," *IEEE Trans. Med. Imag.*, vol. 22, no. 5, pp. 627–635, May 2003.

[8] S. Hermann, K. L. Helmut, and R. Javier, "Magnetic induction tomography: Hardware for multi-frequency measurements in biological tissues," *Physiol. Meas.*, vol. 22, no. 1, pp. 131–146, 2001.

[9] D. Gürsoy and H. Scharfetter, "Imaging artifacts in magnetic induction tomography caused by the structural incorrectness of the sensor model," *Meas. Sci. Technol.*, vol. 22, no. 1, Dec. 2011, Art. no. 015502.

[10] C. Deans, L. Marmugi, S. Hussain, and F. Renzoni, "Electromagnetic induction imaging with a radio-frequency atomic magnetometer," *Appl. Phys. Lett.*, vol. 108, no. 10, Mar. 2016, Art. no. 103503.

[11] K. Stawicki, S. Gratkowski, M. Komorowski, and T. Pietrusewicz, "A new transducer for magnetic induction tomography," *IEEE Trans. Magn.*, vol. 45, no. 3, pp. 1832–1835, Mar. 2009.

[12] C. Tan, Y. Wu, Z. Xiao, and F. Dong, "Optimization of dual frequency-difference MIT sensor array based on sensitivity and resolution analysis," *IEEE Access*, vol. 6, pp. 34911–34920, 2018.

[13] H.-Y. Wei and M. Soleimani, "Hardware and software design for a national instrument-based magnetic induction tomography system for prospective biomedical applications," *Physiol. Meas.*, vol. 33, no. 5, pp. 863–879, Apr. 2012.

[14] J. R. Feldkamp, "Single-coil magnetic induction tomographic three-dimensional imaging," *J. Med. Imag.*, vol. 2, no. 1, Mar. 2015, Art. no. 013502.

[15] C. A. González, C. Villanueva, C. Vera, O. Flores, R. D. Reyes, and B. Rubinsky, "The detection of brain ischaemia in rats by inductive phase shift spectroscopy," *Physiol. Meas.*, vol. 30, pp. 809–819, Jun. 2009.

[16] G. Jin, J. Sun, M. Qin, Q. Tang, L. Xu, X. Ning, J. Xu, X. Pu, and M. Chen, "A new method for detecting cerebral hemorrhage in rabbits by magnetic inductive phase shift," *Biosensors Bioelectron.*, vol. 52, no. 4, pp. 374–378, 2014.

[17] S. Zhao, G. Li, S. Gu, J. Ren, J. Chen, L. Xu, M. Chen, J. Yang, K. W. Leung, and J. Sun, "An experimental study of relationship between magnetic induction phase shift and brain parenchyma volume with brain edema in traumatic brain injury," *IEEE Access*, vol. 7, pp. 20974–20983, Feb. 2019.

[18] M. Soleimani, W. R. B. Lionheart, and A. J. Peyton, "Image reconstruction for high-contrast conductivity imaging in mutual induction tomography for industrial applications," *IEEE Trans. Instrum. Meas.*, vol. 56, no. 5, pp. 2024–2032, Oct. 2007.

[19] L. Ma, S. Spagnul, and M. Soleimani, "Metal solidification imaging process by magnetic induction tomography," *Sci. Rep.*, vol. 7, no. 1, Nov. 2017, Art. no. 14502.

[20] Y. Zhou, Q. Ma, G. Guo, J. Tu, and D. Zhang, "Magneto-acousto-electrical measurement based electrical conductivity reconstruction for tissues," *IEEE Trans. Biomed. Eng.*, vol. 65, no. 5, pp. 1086–1094, May 2018.

[21] L. Wang and A. M. Al-Jumaily, "Imaging of lung structure using holographic electromagnetic induction," *IEEE Access*, vol. 5, pp. 20313–20318, 2017.

[22] R. Merwa, K. Hollaus, B. Brandstätter, and H. Scharfetter, "Numerical solution of the general 3D eddy current problem for magnetic induction tomography (spectroscopy)," *Physiol. Meas.*, vol. 24, no. 2, pp. 545–554, Apr. 2003.

[23] L. Ma and M. Soleimani, "Magnetic induction tomography methods and applications: A review," *Meas. Sci. Technol.*, vol. 28, no. 7, Jun. 2017, Art. no. 072001.

[24] Q. Wang, *Practical Design of Magnetostatic Structure Using Numerical Simulation*. Hoboken, NJ, USA: Wiley, 2013.

[25] N. De Geeter, G. Crevecoeur, and L. Dupré, "An efficient 3-D eddy-current solver using an independent impedance method for transcranial magnetic stimulation," *IEEE Trans. Biomed. Eng.*, vol. 58, no. 2, pp. 310–320, Feb. 2011.

[26] Z. Xiao, C. Tan, and F. Dong, "Effect of inter-tissue inductive coupling on multi-frequency imaging of intracranial hemorrhage by magnetic induction tomography," *Meas. Sci. Technol.*, vol. 28, no. 8, Jul. 2017, Art. no. 084001.

[27] F. Wu, J. Jeon, S. K. Moon, H. J. Choi, and H. Son, "Voice coil navigation sensor for flexible silicone intubation," *IEEE/ASME Trans. Mechatronics*, vol. 21, no. 2, pp. 851–859, Apr. 2016.

[28] F. Wu, S. K. Moon, and H. Son, "Orientation measurement based on magnetic inductance by the extended distributed multi-pole model," *Sensors*, vol. 14, pp. 11504–11521, Jun. 2014.

[29] J. Jeon and H. Son, "Active control of magnetic field using eDMP model for biomedical applications," *IEEE/ASME Trans. Mechatronics*, vol. 23, no. 1, pp. 29–37, Feb. 2018.

[30] P. A. Hasgall. (May 15, 2018). *IT'IS Database for Thermal and Electromagnetic Parameters of Biological Tissues*. [Online]. Available: http://itis.swiss/database

JIYUN JEON received the B.S. degree in mechanical and nuclear engineering from the Ulsan National Institute of Science and Technology (UNIST), Ulsan, South Korea, in 2014, where she is currently pursuing the Ph.D. degree with the School of Mechanical, Aerospace and Nuclear Engineering. Her research interests include magnetic sensors, magnetic induction tomography, and magnetic field design.

WONMO CHUNG received the B.S. degree in mechanical and nuclear engineering from the Ulsan National Institute of Science and Technology (UNIST), Ulsan, South Korea, in 2016, where he is currently pursuing the Ph.D. degree with the School of Mechanical, Aerospace and Nuclear Engineering. His research interests include magnetic sensors, magnetic induction tomography, and robust control of UAV.

HUNGSUN SON (S'07–M'09) received the M.S. degree in aero and astronautical engineering from Stanford University, Stanford, CA, USA, in 2002, and the Ph.D. degree in mechanical engineering from the Georgia Institute of Technology, Atlanta, in 2007. He is currently an Associate Professor in mechanical, aerospace, and nuclear engineering with the Ulsan National Institute of Science and Technology (UNIST), South Korea. His current research interests include mechatronics, sensors and actuators, dynamic system modeling, design optimization, automation, and control.